ORIGINAL ARTICLE

S.C. Jayswal · V.K. Jain · P.M. Dixit

Modeling and simulation of magnetic abrasive finishing process

Abstract Magnetic abrasive finishing (MAF) is one of the advanced finishing processes, which produces a high level of surface quality and is primarily controlled by a magnetic field. In MAF, the workpiece is kept between the two poles of a magnet. The working gap between the workpiece and the magnet is filled with magnetic abrasive particles. A magnetic abrasive flexible brush (MAFB) is formed, acting as a multipoint cutting tool, due to the effect of the magnetic field in the working gap. This paper deals with the theoretical investigations of the MAF process. A finite element model of the process is developed to evaluate the distribution of magnetic forces on the workpiece surface. The MAF process removes a very small amount of material by indentation and rotation of magnetic abrasive particles in the circular tracks. A theoretical model for material removal and surface roughness is also proposed accounting for microcutting by considering a uniform surface profile without statistical distribution. Numerical experiments are carried out by providing different routes of intermittent motion to the tool. The simulation results are verified by comparing them with the experimental results available in the literature.

Keywords FEM · Magnetic abrasive finishing (MAF) ·
Modeling · Nanometer (nm) finish ·
Non-conventional finishing · Simulation

1 Introduction

Traditional fine finishing operations such as grinding, lapping, or honing employ a rigid tool that subjects the workpiece to substantial normal stresses which may cause microcracks resulting in reduced strength and reliability of the machined part. A rela-

S.C. Jayswal* · V.K. Jain (✉) · P.M. Dixit
Department of Mechanical Engineering,
Indian Institute of Technology Kanpur,
Kanpur-208016, India
E-mail: vkjain@iitk.ac.in
*On leave from Department of Mechanical Engineering, M.M.M. Engineering college, Gorakhpur-273010, India

tively new fine finishing method, magnetic abrasive finishing (MAF) is an advanced finishing process in which the cutting force is primarily controlled by the magnetic field. It minimizes the possibility of microcracks on the surface of the workpiece, particularly in hard brittle material, due to controlled low forces acting on abrasive particles [1]. This process is able to produce surface roughness of nanometer range on flat surfaces as well as internal and external cylindrical surfaces [2]. It can also be used for internal finishing of non-rotatable workpieces such as elbows and bent tubes [3]. The MAF process offers many advantages, such as self-sharpening, self-adaptability, controllability, and the finishing tools require neither compensation nor dressing [4].

In MAF, the workpiece is kept between the two poles of a magnet (Fig. 1a). The working gap between the workpiece and the magnet is filled with magnetic abrasive particles (MAPs) (Fig. 2), composed of ferromagnetic particles and abrasive powder. MAPs can be used as bonded or unbonded. Bonded MAPs are prepared by sintering of ferromagnetic particles and abrasive powder whereas unbonded MAPs are a mechanical mixture of ferromagnetic particles and abrasive powder with a small amount of lubricant [4–6]. The purpose of the lubricant is to provide some holding strength between the constituents of MAPs. The bonded type of MAPs are considered in the present work due to their excellent finishing effects [4]. The magnetic abrasive particles join each other along the lines of magnetic force and form a magnetic abrasive flexible brush (MAFB) between the workpiece and the magnetic pole (Fig. 1a). This brush behaves like a multi-point cutting tool for the finishing operation. When the magnetic N-pole is rotating, the MAFB also rotates like a flexible grinding wheel and finishing is done according to the forces acting on the abrasive particles. It is usually assumed that there is no slip between the N-pole and MAFB. The arrangement of magnetic abrasive particles is shown only in the last track (Fig. 1b), however, in reality many such tracks are formed on the workpiece.

Shinmura et al. [7, 8] found that magnetic flux density and working gap greatly affect the surface roughness and stock removal. A vibrational motion given to cylindrical workpieces enhances the finishing efficiency. Shinmura et al. [6, 9] have also analyzed the effect of the size of magnetic abrasive particles, and

Line of magnetic force

Magnetic equipotential line

Magnetic abrasive particle

Workpiece

Rotation

N-pole

S pole

a

Periphery of N-pole

Magnetic abrasive particles

Track width

Circular

Radius of magnetic abrasive brush

Workpiece

b

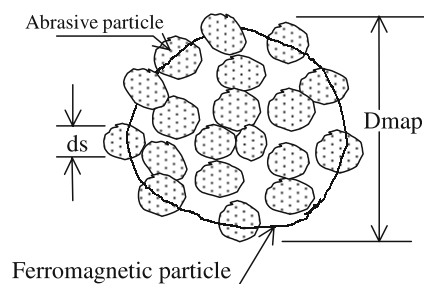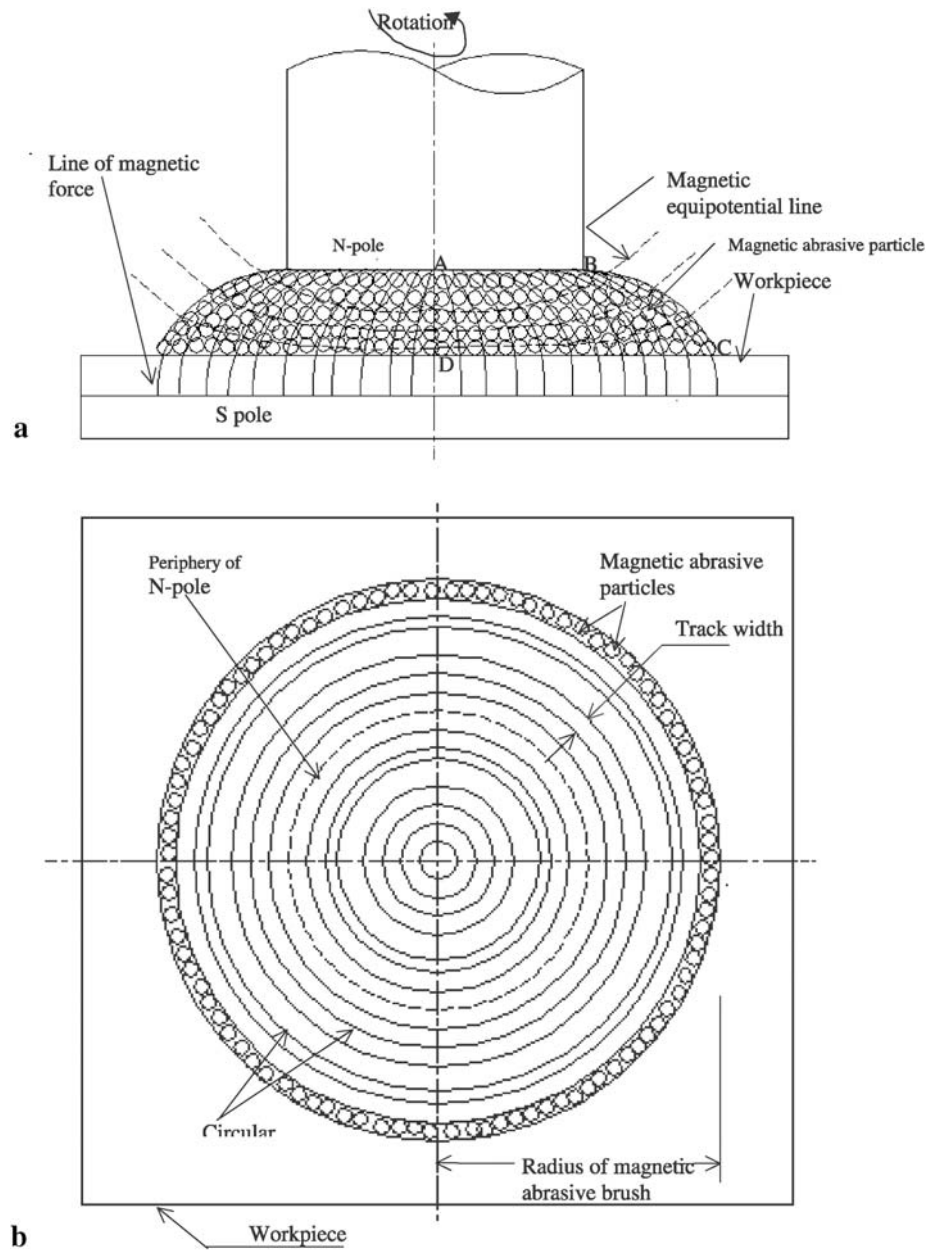Abrasive particle

ds

Dmap

Ferromagnetic particle

Fig. 2. Schematic view of a bonded magnetic abrasive particle; D_{map} = Diameter of magnetic abrasive particle; ds = diameter of abrasive particle

found that stock removal and surface roughness value increase as the magnetic abrasive particle diameter "Dmap" increases. Surface roughness is improved by decreasing the abrasive particle diameter "ds". Deburring of grinding burrs can easily be performed with this process. Fox et al. [10] have found that unbonded MAPs yield a higher material removal rate (MRR) and bonded MAPs give a better surface roughness. The surface roughness value (Ra) of a ground rod after MAF has been achieved as low as 10 nm. It was observed during finishing the external surface of a cylindrical workpiece by Jain et al. [2], that the working gap and circumferential speed of the workpiece are the parameters which significantly influence material removal and the change in surface roughness value.

Shinmura et al. [11, 12] have also conducted an experimental study on plane workpieces using the MAF process. They observed that the surface roughness value decreases with increasing finishing time upto a certain limit of time beyond which no further improvement was noticed. Addition of machining fluid (such as stearic acid, straight oil type of grinding fluid) to unbonded MAPs has shown remarkable effects on stock removal and surface roughness [5].

Hou et al. [13] presented the thermal aspect of magnetic abrasive finishing of a ceramic roller using the bonded type of MAPs. Waigaonkar et al. [14] presented the optimization of the magnetic abrasive process. Yamguchi et al. [15] developed an internal magnetic abrasive finishing process using a pole rotation system to produce a highly finished inner surface of a workpiece. They also studied the effect of a magnetic field on MAFB configuration and force acting on abrasive particles.

Kremen et al. [16] developed an empirical expression to estimate machining time to produce a workpiece with specified out-of-roundness. Kim and Choi [17] modeled and simulated the MAF process for finishing cylindrical workpieces and concluded that the magnetic flux density in the air-gap is affected greatly by the length of the air-gap; magnetic flux density increases as the air-gap length decreases. They have also found that simulation results for surface roughness agree better with the experimental data for the low magnetic flux density than they do for high magnetic flux density. Kremen et al. [18] proposed a theory to explain the "out-of-roundness" phenomenon based on force analysis and the material removal mechanism.

From the above literature survey, it can be concluded that very little effort has been made toward the modeling and simulation of the plane magnetic abrasive finishing process. Most of the work done on this process is experimental and consists of the study of the process principle and effects of various process parameters on the material removal and surface roughness. This paper presents a mathematical model for mechanics of material removal during the MAF process. A theoretical model of surface roughness has also been proposed to predict surface quality. To determine surface quality, distribution of magnetic forces needs to be estimated first. A finite element based code has been developed to evaluate the distribution of magnetic forces, considering magnetic flux density, type and size of MAPs, and the working gap as the main parameters.

2 Mathematical modeling

The MAF process is not completely understood as there is a lack of quantitative relationships between process parameters and process performance. Mathematical modeling and analysis of the process would help in understanding the forces acting on the workpiece and mechanism of material removal.

In MAF, magnetic abrasive particles are placed under the influence of a magnetic field. MAPs acquire magnetic polarization and join each other along the lines of magnetic force, forming a magnetic abrasive flexible brush. The MAF process involves irregular geometry in the working gap and nonlinear composite material properties of the MAFB. Use of analytical methods to obtain the solution of the governing equation under such heterogeneous conditions would be very difficult. Therefore, the finite element method is used to obtain the solution. Here, the governing equation of the process is expressed in terms of the magnetic potential, which is the primary variable.

2.1 Governing equation

The following assumptions are made to derive the governing equation which is based on Maxwell's equations [19]:

1. The intensity of the magnetic field is not varying with time as the operating parameters are held constant during MAF process.
2. Leakage of the magnetic field, if any, is negligible due to a small working gap.
3. When the magnetic field is applied, the magnetic abrasive particles are closely packed in the form of a brush between the tool (north pole) and workpiece. It means that there is no air pocket in the brush, and relative permeability of MAPs is calculated by considering relative fractions of ferromagnetic particles and abrasive particles.
4. The chips removed during the MAF process have an insignificant effect on the properties of the MAFB due to very low material removal during the process.
5. The magnetic potential drop in the core is neglected due to very low reluctance of the core.
6. The solution domain is considered as axisymmetric because of the axisymmetic nature of the geometry of the MAFB as shown in Fig. 1b and magnetic field.

Intensity of the magnetic field $\mathbf{H}$ is a gradient of magnetic scalar potential ϕ and is expressed as:

$$\mathbf{H} = -\nabla\phi . \tag{1}$$

Based on the above assumptions, in the axisymmetric form, the governing equation of the process becomes:

$$\frac{1}{r}\frac{\partial}{\partial r}\left[r\mu_r\frac{\partial\phi}{\partial r}\right] + \frac{\partial}{\partial z}\left[\mu_r\frac{\partial\phi}{\partial z}\right] = 0 , \tag{2}$$

where, ϕ is a magnetic scalar potential and μ_r is the relative permeability of MAPs. The permeability of most of the ferromagnetic materials is not constant, and varies with the magnetic field. It implies that Eq. 2 is non-linear in nature.

2.2 Boundary conditions

Since the problem is axisymmetric, only the right half of the cross section (region ABCD of Fig. 1a) is used as a solution domain for the analysis. The solution domain is shown in Fig. 3. The total boundary consists of four parts: C_1, C_2, C_3, and C_4. The boundary conditions of the problem are as follows.

(1) Essential boundary conditions:
The magnetic potential ϕ is specified on the boundaries C_1 and C_3 (Fig. 3). The magnetic potential is assumed to have a zero
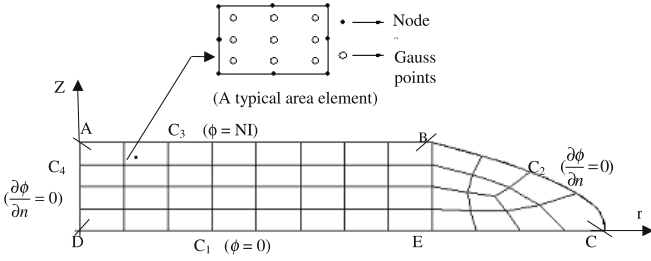
Fig. 3. Finite element mesh

value at the workpiece (C_1-south pole). The value of magnetic potential on the north pole (C_3) can be calculated as a product of input current (I) and the number of turns (N) in the electromagnet (due to assumptions 2 and 5). Thus,

$$\phi = 0 \quad \text{on} \quad C_1 , \tag{3}$$

$$\phi = NI \quad \text{on} \quad C_3 . \tag{4}$$

(2) Natural boundary conditions:

On the line of symmetry (AD) (Fig. 3), the normal derivative of the magnetic potential is zero. Thus,

$$\frac{\partial \phi}{\partial n} = 0 \quad \text{on} \quad C_4 . \tag{5}$$

The boundary BC is a line of magnetic force. Then the equipotential lines are perpendicular to this boundary. Therefore, the normal derivative of the magnetic potential is zero on the boundary BC. Thus,

$$\frac{\partial \phi}{\partial n} = 0 \quad \text{on} \quad C_2 \tag{6}$$

The shape of this line BC and the location of point C are unknown. In this work, the boundary BC is approximated as a parabola and the location of point C is found by the trial and error method. For this purpose numerical experiments were performed by varying the length of the fringing zone from one to six times the working gap. When EC is equal to two times the working gap, magnetic potential is just 0.2% in comparison to its maximum value. Hence, the distance EC (Fig. 3) is taken as being equal to twice the working gap (BE).

3 Finite element analysis

Galerkin's finite element method [20] is used to evaluate the distribution of magnetic potential (ϕ) within the solution domain. The domain is discretised using an isoparametric eight noded quadrilateral elements (Fig. 3).

3.1 Finite element equations and solution procedure

Application of the Galerkin finite element method to the problem consisting of differential Eq. 3 and boundary conditions (Eqs. 3–6) leads to the following algebraic equations:

$$[K]\{\phi\} = \{0\} , \tag{7}$$

where the vector $\{\phi\}$, called the global magnetic potential vector, contains the nodal value of ϕ at all the nodes of the domain and the matrix $[K]$, called the global coefficient matrix. The value of $[K]$ is obtained after assembling the elemental coefficient matrices over all the elements. The typical elemental coefficient matrix $[k]^e$ is given by

$$[k]^e = \int_{A_e} \mu_r [B]^{eT} [B]^e 2\pi r \, dr dz , \tag{8}$$

where the matrix $[B]^e$ contains derivatives of the shape functions and A_e is the domain of a typical area element.

The integral in expression 8 is computed numerically using the Gauss–Legendre quadrature with 3 Gauss points in each direction. The value of μ_r of MAPs depends on the field strength which, in turn, depends on the magnetic scalar potential. Therefore, the values of μ_r at the Gauss points are found iteratively. The relations between μ_r and $\mathbf{H}$ (graphical as well as in the form of equations) are given in Appendix-I. The variation (ε) in the solution in the consecutive iterations is computed as

$$\varepsilon = \frac{\sqrt{\sum_{i=1}^{tnn} \left| \phi_i^{(k)} - \phi_i^{(k-1)} \right|^2}}{\sqrt{\sum_{i=1}^{tnn} \left(\phi_i^{(k-1)} \right)^2}} , \tag{9}$$

where tnn is the total number of nodes and k is iteration number. Iterations are continued till the value of ε is equal to or less than the prescribed tolerance (say, equal to 10^{-3}).

The finite element equations (Eq. 7) are a set of linear algebraic equations. These equations are solved by the Gauss elimination method after imposing essential boundary conditions.

3.2 Evaluation of secondary variables

The values of secondary variables are most accurate at the Gauss points. Therefore intensity of the magnetic field, derivative of intensity of magnetic field, and magnetic force are calculated at the Gauss points. For the calculation of magnetic forces, $\mathbf{H}$ and its derivatives are needed. These are calculated from Eq. 1 using the finite difference method [21].

The magnetic force on a particle depends on the magnetic field strength and the magnetic property of the particle. By virtue of its position in the magnetic field, the magnetic potential energy, E_m, of the particle is given by Eq. 10 [22]:
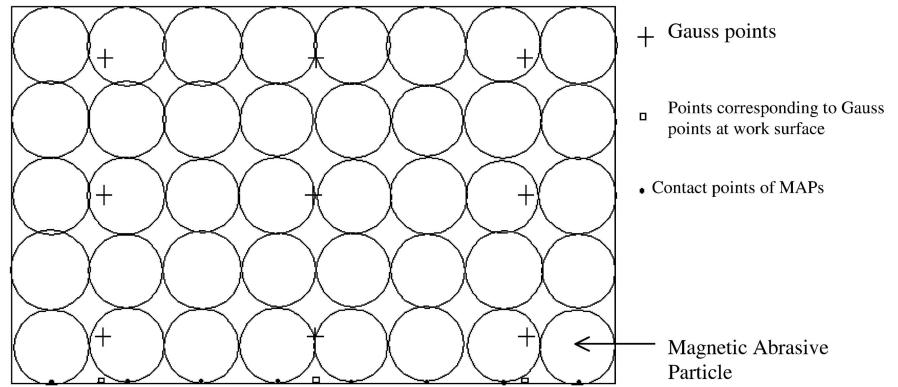
$$E_m = \frac{\mu_0}{2} \int_v \chi_r \mathbf{H} \cdot \mathbf{H} \, dv , \tag{10}$$

where, v is the volume of the particle and χ_r is its susceptibility. The magnetic force $\mathbf{F}$ acting on the particle is defined as the gradient of the magnetic potential energy. The radial and normal components of $\mathbf{F}$ can be expressed as

$$F_r = \frac{\mu_0}{2} v \frac{\partial}{\partial r} (\chi_r \mathbf{H} \cdot \mathbf{H}) , \tag{11}$$

$$F_z = \frac{\mu_0}{2} v \frac{\partial}{\partial z} (\chi_r \mathbf{H} \cdot \mathbf{H}) . \tag{12}$$

Fig. 4. A typical element with MAPs

Since the magnetic abrasive particle is composed of ferromagnetic particles and abrasive particles, according to Wiedemann's law [23], its susceptibility can be expressed as

$$\chi_r = \alpha\chi_{r\,ferr} + (1-\alpha)\chi_{rabr} , \qquad (13)$$

where α is the volume fraction of ferromagnetic particles, and $\chi_{r\,ferr}$ and χ_{rabr} are the susceptibilities of ferromagnetic material and abrasive particles, respectively.

From the known values of the intensity of the magnetic field and its derivatives at the Gauss points, the magnetic forces are calculated first at the Gauss points of the elements in contact with the workpiece surface. Then, they are extrapolated on the points indicated by □ in Fig. 4. Further, extrapolation or interpolation at the contact surface is necessary to determine magnetic forces at the actual contact points between the MAPs and the work surface. For this, the locations of the actual contact points of MAPs need to be determined. This is discussed in the following paragraph.

In the present work, the tool (N-pole) is cylindrical and the workpiece surface is flat. Therefore, the cross sectional area of the brush is circular. It is assumed that MAPs are closely packed in the gap and rotate in a particular track as shown in Fig. 1b. The location of the contact point of a MAP depends on the radius of the track, in which the particle rotates. The location of a contact point is, therefore, given by

$$R_{(tr)} = (tr - 1)\,D_{map} + \frac{D_{map}}{2} , \qquad (14)$$

where $R_{(tr)}$ is radius of the tr-th track and D_{map} is diameter of the magnetic abrasive particle (assumed to be the same for each MAP). The total number of tracks (n_t) in a brush is given by

$$n_t = \frac{\text{radius of magnetic abrasive brush}}{D_{map}} , \qquad (15)$$

The radius of the magnetic abrasive brush at the workpiece interface is equal to the length DC of Fig. 1 and D_{map} is shown in Fig. 2 (or width of a track in Fig. 1b).

4 Material removal and surface roughness

The mechanism of material removal is based on microcutting [17]. The MAF process removes material in the form of tiny chips. The volume of these chips is equal to the volume of grooves produced on the workpiece surface during the MAF process. Magnetic and mechanical energies are utilized in the MAF process. A magnetic abrasive flexible brush is formed due to the effect of a magnetic field in the working gap. The rotation of the north pole makes the MAFB rotate. It generates the tangential force (F_t) on the cutting edges of MAPs. The magnetic energy develops the normal (F_z) and radial (F_r) magnetic forces on the MAPs. The normal magnetic force creates compressive reaction on the surface of the workpiece. This compressive force is responsible for the penetration of cutting edges into the workpiece. The resultant of radial magnetic force and mechanical tangential force on the cutting edges of MAPs removes (shears out) the material from the workpiece along the circular paths. It is assumed that the total mechanical power available at the end of the spindle (N pole) is utilized in finishing the workpiece. The tangential force, which removes material from the workpiece, is assumed to be uniformly distributed. In the present case, it is assumed that all the cutting edges work simultaneously. Therefore, finishing power is the summation of the product of the tangential force and cutting speed on each cutting edge.

Total number of cutting edges ($n_{ct(tr)}$) in the tr-th track is given by

$$n_{ct(tr)} = \frac{2\pi R_{(tr)}\,n_a}{D_{map}} , \qquad (16)$$

where n_a is the number of active cutting edges of the MAPs (assumed to be 1 in this particular case). Cutting speed of a particle in the tr-th track ($Vc_{(tr)}$) is given by

$$Vc_{(tr)} = 2\pi R_{(tr)} N_{rs} , \qquad (17)$$

where N_{rs} is the rotational speed of the magnetic pole. Thus, the finishing power is given by

$$P = \sum_{tr=1}^{n_t} F_{tedge}\left(n_{ct(tr)} Vc_{(tr)}\right) , \qquad (18)$$

where F_{tedge} is the tangential force on the cutting edge. Substituting the value of $n_{ct(tr)}$ from Eq. 16 and $Vc_{(tr)}$ from Eq. 17 in Eq. 18, the tangential force is given by

$$F_{tedge} = \frac{P}{\sum\limits_{tr=1}^{n_t} \left(\frac{4\pi^2 R_{(tr)}^2 N_{rs} n_a}{D_{map}} \right)} . \tag{19}$$

The cutting force (F_c) is resultant of tangential force (F_t) and radial force (F_r):

$$F_c = \sqrt{F_t^2 + F_r^2} . \tag{20}$$

Total tangential force and radial force on the MAFB for the specified machining conditions, are found to be 97.6368 N and 2.5285 N, respectively. Therefore the resultant cutting force (F_c) is given by

$$F_c = \left(\sqrt{97.6368^2 + 2.5385^2} \right) N = 97.6695 \, N . $$

Since the overall effect of the radial force is negligible, the cutting force on the edge (F_{cedge}) can be taken as equal to the tangential force (F_{tedge}).

The force required (F_{req}) to remove material from the workpiece depends on the shear strength (τ_s) of the workpiece material and projected area of the penetration (A_p in Fig. 5c). Thus,

$$F_{req} = \tau_s A_p . \tag{21}$$

In removing the material in the MAF process, one of the three situations may occur:

(1) $F_{req} = F_{cedge}$
It is the equilibrium condition. It indicates starting of the finishing operation.
(2) $F_{req} < F_{cedge}$
Under this condition, material is removed.
(3) $F_{req} > F_{cedge}$

It shows no cutting condition. Under this condition, the depth of penetration of the cutting edge gets adjusted by rotation of the magnetic abrasive particle until the cutting force required becomes equal to the cutting force available F_{cedge}, keeping the cross sectional area of indentation (A_i) the same as shown in Fig. 6:

$$\bar{F}_{req} = F_{cedge} , \tag{22}$$

where $\bar{F}_{req}$ is the modified required cutting force:

$$\bar{F}_{req} = \tau_s A_p' , \tag{23}$$

where A_p' is the modified projected area of penetration. Substituting the value of $\bar{F}_{req}$ from Eq. 22 in Eq. 23, we get

$$A_p' = \frac{F_{cedge}}{\tau_s} . \tag{24}$$

Assumptions

For simplification of computational work, the following assumptions are made in developing the model for material removal and surface roughness:

1. The surface of the workpiece has a uniform triangular profile.

Fig. 5a–c. Schematic diagram of abrasive grain showing: **a** Depth of penetration **b** Projected area of indentation **c** Projected area of penetration
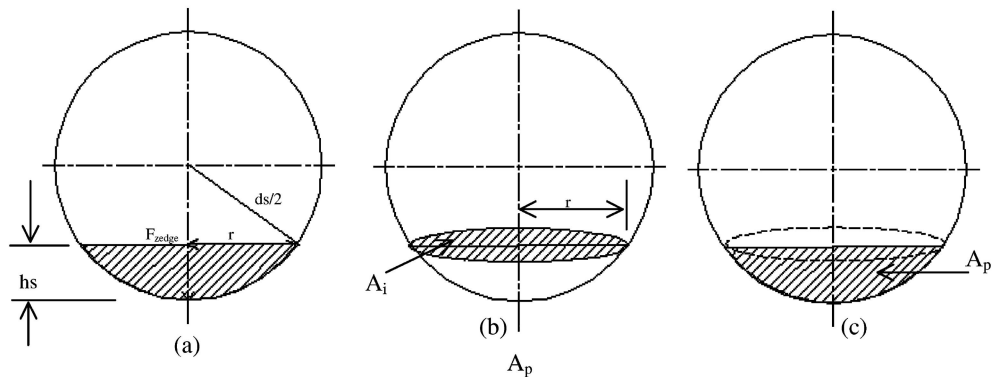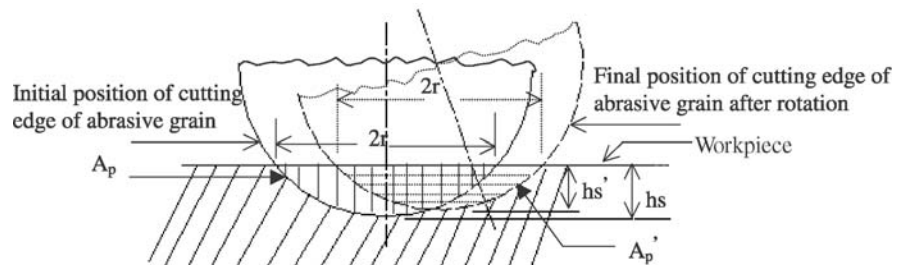
Fig. 6. Rotation of a magnetic abrasive particle. hs = depth of penetration before rotation, hs′ = depth of penetration after rotation, A_p = projected area of penetration before rotation, A_p' = projected area of penetration after rotation

2. There is no relative motion between the MAPs because these are arranged closely along the lines of the magnetic force in the form of a semi-rigid brush. This results in insignificant porosity in the brush between the particles.

3. The shape of MAPs is approximated to be spherical and of the same size. Only one cutting edge of the MAP is assumed to be in contact with the the workpiece. This cutting edge of a MAP in contact with the workpiece removes material in its own track. Each cutting edge of a particular track removes the same amount of material.

4. To render the problem mathematically tractable, it is necessary to assume that the working gap remains constant during finishing.

5. The size of the magnetic abrasive particle is larger than the spacing between the two consecutive peaks of surface unevenness because the MAF process is applied for finishing the semi finished components, having the spacing of the order of a few micrometer.

6. There is no slip between the rotating spindle (N pole) and the MAFB due to the force of magnetic attraction between them.

4.1 Material removal model

MAF process removes a very small amount of material by penetration and rotation of MAPs on the work surface to be finished. The volume of material removed by an abrasive grain is equal to the product of sheared area and length of finishing of the workpiece (ie., the length of contact of the abrasive grain on the workpiece surface).

The normal magnetic force on the abrasive particles causes penetration into the workpiece. The normal force acting on a cutting edge (F_{zedge}) of the magnetic abrasive particle is given as

$$F_{zedge} = \frac{F_z}{n_a}, \tag{25}$$

where F_z is the normal magnetic force acting on the MAP. The depth of penetration is calculated by equating the applied force to the reaction of the workpiece [24]:

$$F_{zedge} = H_m , \Delta A \tag{26}$$

where H_m is hardness of the workpiece material and ΔA is the projected area of indentation (shaded area of Fig. 5b). The projected area of indentation is circular. Let, r be the radius of this circular area. Then, r is given by

$$r = \sqrt{\frac{F_{zedge}}{H_m \pi}} . \tag{27}$$

From the geometry of Fig. 5a, the depth of penetration (hs) is obtained as

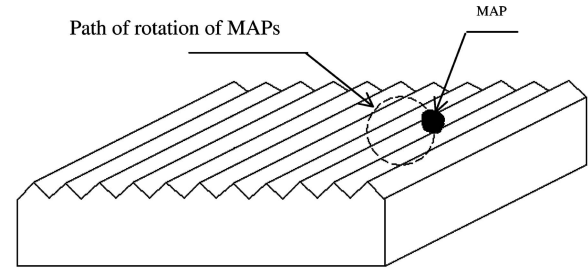$$hs = \frac{ds}{2} - \sqrt{\left(\frac{ds}{2}\right)^2 - r^2}, \tag{28}$$

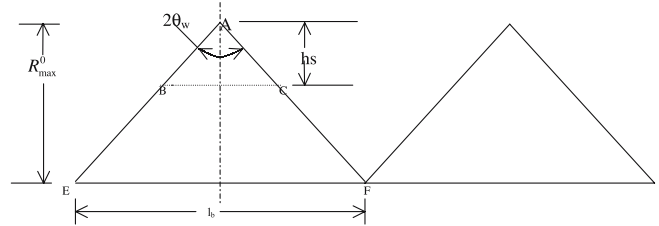**Fig. 7.** Schematic diagram of workpiece surface profile

Fig. 8. Shape of the surface profile

where, ds is the diameter of the abrasive particle. Substituting the value of "r" from Eq. 27, we get

$$hs = \frac{ds}{2} - \sqrt{\left(\frac{ds}{2}\right)^2 - \frac{F_{zedge}}{H_m \pi}} . \tag{29}$$

The projected area (A_p) of penetration subjected to the shearing force during the MAF (shaded area of Fig. 5c) as obtained from the geometry of Fig. 5a is

$$Ap = \frac{(ds)^2}{4} \left[\cos^{-1}\left(1 - \frac{2hs}{ds}\right) \right] - \left(\left(\frac{ds}{2} - hs\right) \sqrt{hs(ds - hs)} \right) . \tag{30}$$

Figure 7 shows a schematic diagram of the assumed workpiece surface profile along with the path (or track) of rotation of a MAP, which is circular. The cutting edges of MAPs in contact with the workpiece remove the material along the circular path. However, the brush is provided intermittent feed after completion of each revolution of the brush/pole. Therefore, the location of each MAP varies with respect to the surface of the workpiece after each revolution. To simplify the computation of material removal and surface roughness, the workpiece surface is divided in small square cells. The cell is specified by the Cartesian coordinates of its center. It is assumed that material in the cell is removed by the MAP whose track passes through the cell. The procedure to calculate the material removal is as follows. The flow chart for computation of material removal and surface roughness is given in Appendix-II.

Let the initial surface roughness of the workpiece be R_{max}^0. The volume of material removed by a MAP passing through the cell (i,j) in the nth revolution is

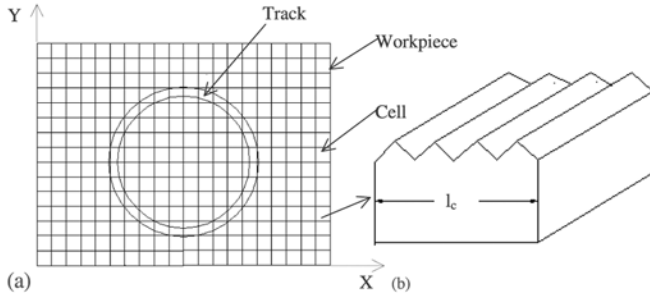$$\Delta V_{ed(i,j))}^{(n)} = Ap_{(tr)} l_{t(i,j)}^{(n)}, \tag{31}$$

Fig. 9. a Schematic diagram of workpiece with cells, **b** Exaggerated view of a typical cell

where $Ap_{(tr)}$ is the sheared area in track "tr" as discussed earlier (Eq. 30) and $l^{(n)}_{t(i,j)}$ is the length of contact of the MAP with the surface of the cell (i,j) in the nth revolution. The length of contact of the MAP in cell (i,j) is the product of the contact length of a single profile $\left(l^{(n)}_{(i,j)}\right)$ and the number of profiles (n_f) in the cell (i,j).

$$l^{(n)}_{t(i,j)} = l^{(n)}_{(i,j)} n_f . \tag{32}$$

From Fig. 8, the contact length (BC) of a single profile can be obtained as

$$l^{(n)}_{(i,j)} = 2hs^{(n)}_{(tr)} \tan \theta_w , \tag{33}$$

where $hs^{(n)}_{(tr)}$ is the depth of penetration of the MAP in the tr-th track and $2\theta_w$ is the mean angle of surface asperity. The mean angle of surface asperity depends upon the initial surface roughness and manufacturing process of the work surface. Figure 9a shows the work surface divided into various cells. An exaggerated view of a typical cell is shown in Fig. 9b. Here, it is also assumed that each grain cuts the peaks normal to its lay direction. From Fig. 9b, we get

$$n_f = \frac{l_c}{l_b} , \tag{34}$$

where l_c is the length of cell and l_b is the base length of a single profile. From Fig. 8, l_b is given by

$$l_b = 2R^0_{max} \tan \theta_w . \tag{35}$$

Substituting Eqs. 32–35 into Eq. 31, we get

$$\Delta V^{(n)}_{ed(i,j)} = \frac{Ap_{(tr)} hs^{(n)}_{(tr)} l_c}{R^0_{max}} . \tag{36}$$

The total volume of material removed in a cell (i,j) in the nth revolution is

$$\Delta V^{(n)}_{(i,j)} = \Delta V^{(n)}_{ed(i,j)} n_{ct(tr)} . \tag{37}$$

Substituting the value of $\Delta V^{(n)}_{ed(i,j)}$ from Eq. 36 and $n_{ct(tr)}$ from Eq. 16 in Eq. 37

$$\Delta V^{(n)}_{(i,j)} = \frac{2Ap_{(tr)} hs^{(n)}_{(tr)} l_c \pi R_{(tr)} n_a}{R^0_{max} D_{map}} . \tag{38}$$

To compute the total material removed in each cycle, the material removed in each cell can be summed up. The total material removed in the nth rotation is given by

$$\Delta V^{(n)} = \sum \Delta V^{(n)}_{(i,j)} . \tag{39}$$

4.2 Surface roughness model

The MAF process improves surface quality by reducing the unevenness of the surface profile. The normal magnetic force applies machining pressure on the workpiece surface through MAPs, resulting in the penetration of cutting edges of abrasive grains in the workpiece. Due to rotation of MAPs, grooves are formed on the workpiece surface which decide the surface profile after the MAF. Surface roughness is determined on the basis of the surface profile achieved by equating the volume of the material removed to the volume of groove produced. It is assumed that the surface of the workpiece has uniform triangular profiles (Fig. 8) without statistical distribution. Initial surface roughness is R^0_{max} and after completion of "n" revolutions of the MAFB, surface roughness in cell (i,j) becomes $R^{(n)}_{max(i,j)}$. Volume of the groove produced in a profile is equal to the product of the cross sectional area of the removed portion of the surface profile and average width of cut. The average width of cut is equal to the radius of the projected area of penetration of the abrasive grain (Sect. 4.1), in that profile. The cross sectional area of the removed portion of surface profile varies in each revolution as shown in Fig. 10.

From the geometry of the profile of a workpiece surface as shown in Fig. 10, AD, BC and the volume of the groove produced in one profile in a cell (i,j) by a cutting edge $\left(\Delta Vg^{(1)}_{ed(i,j)}\right)_{pr}$ are given by

$$AD = R^0_{max} - R^{(1)}_{max(i,j)} \tag{40}$$

$$BC = 2\left(R^0_{max} - R^{(1)}_{max(i,j)}\right) \tan \theta_w \tag{41}$$

$$\left(\Delta Vg^{(1)}_{ed(i,j)}\right)_{pr} = \frac{1}{2} \times AD \times BC \times \left(r_{(tr)}\right) \tag{42}$$

where $r_{(tr)}$ is average width of cut produced by a cutting edge in track "tr". Substituting Eqs. 40 and 41 into Eq. 42, we get

$$\left(\Delta Vg^{(1)}_{ed(i,j)}\right)_{pr} = \left(R^0_{max} - R^{(i)}_{max(i,j)}\right)^2 \tan \theta_w r_{(tr)} . \tag{43}$$

Total volume of the material removed in a cell (i,j) by a cutting edge $\left(\Delta Vg^{(1)}_{ed(i,j)}\right)$ is

$$\Delta Vg^{(1)}_{ed(i,j)} = \left(\Delta Vg^{(1)}_{ed(i,j)}\right)_{pr} n_f . \tag{44}$$

The value of n_f is obtained from Eqs. 34 and 35:

$$n_f = \frac{l_c}{2R^0_{max} \tan \theta_w} . \tag{45}$$

Substituting the value of $\left(\Delta Vg^{(1)}_{ed(i,j)}\right)_{pr}$ from Eq. 43 and n_f from Eq. 45 into Eq. 44,

$$\Delta Vg^{(1)}_{ed(i,j)} = \frac{\left(R^{(0)}_{max} - R^{(1)}_{max(i,j)}\right)^2 r_{(tr)} l_c}{2R^{(0)}_{max}} \tag{46}$$

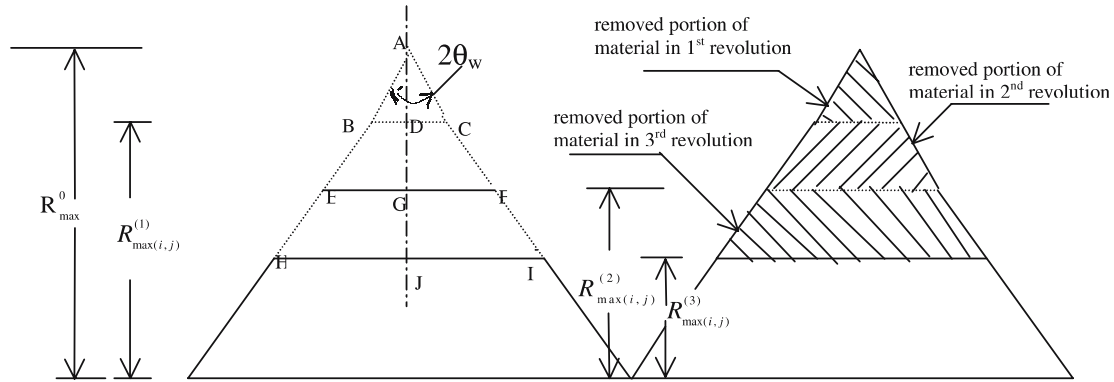**Fig. 10.** Surface profile after 3rd revolution

The total volume of material removed in cell (i,j) by "$n_{(tr)}$" particles is

$$\Delta Vg_{(i,j)}^{(1)} = \Delta Vg_{ed(i,j)}^{(1)} n_{ct(tr)} . \tag{47}$$

Substituting the value of $\Delta Vg_{ed(i,j)}^{(1)}$ from Eq. 46 and $n_{ct(tr)}$ from Eq. 16 into Eq. 47:

$$\Delta Vg_{(i,j)}^{(1)} = \frac{\left(R_{max}^{(0)} - R_{max(i,j)}^{(1)}\right)^2 r_{(tr)} l_c \pi R_{(tr)} n_a}{R_{max}^{(0)} D_{map}} . \tag{48}$$

The volume of material removed in cell (i,j) by "$n_{(tr)}$" particles (as discussed in Sect. 4.1) is equated to the volume of groove produced in that cell in the first revolution:

$$\Delta V_{(i,j)}^{(1)} = \Delta Vg_{(i,j)}^{(1)} . \tag{49}$$

Putting the value of $\Delta Vg_{(i,j)}^{(1)}$ from Eq. 48 into Eq. 49, we get

$$R_{max(i,j)}^{(1)} = R_{max}^{(0)} - \left(\frac{\Delta V_{(i,j)}^{(1)} R_{max}^0 D_{map}}{\pi r_{(tr)} l_c R_{(tr)} n_a}\right)^{\frac{1}{2}}, \tag{50}$$

where $R_{max(i,j)}^{(1)}$ is the surface roughness obtained after one revolution of the N-pole. Following the same procedure (Appendix-III), it can be shown that after the nth revolution, surface roughness in cell (i,j) can be expressed as

$$R_{max(i,j)}^{(n)} = R_{max}^0 - \left(\left(R_{max}^0 - R_{max(i,j)}^{(n-1)}\right)^2 + \left(\frac{\Delta V_{(i,j)}^{(n)} R_{max}^0 D_{map}}{\pi r_{(tr)} l_c R_{(tr)} n_a}\right)\right)^{\frac{1}{2}} . \tag{51}$$

5 Computer implementation

Using the expressions given in Sects. 2–4, a code namely the finite element simulation for magnetic abrasive finishing process

(FEMS-MAFP) has been developed in the Fortran 90 programming language. Results obtained from the code have been presented as follows.

6 Results and discussion

The magnetic forces obtained from the numerical simulation as discussed above, are used for the computation of surface roughness according to the surface roughness model discussed in Sect. 4.2. Then this computed surface roughness is compared with the experimental results of Shinmura et al. [12] to check the validity of the mathematical model and surface roughness model. The machining parameters and material properties employed in the simulation are taken from reference [12] and are given in Table 1.

Before the calculation of magnetic forces, the convergence of mesh is studied. This study has revealed that mesh of 1152 isoparametric eight nodded quadrilateral elements with 3577 nodes are adequate for this problem. The distribution of the normal magnetic force on the workpiece surface along radial direction is shown in Fig. 11. It is found that the magnitude of

Table 1. Machining conditions and material properties

|	
Magnetic flux density (B)	0.8 T
Working gap (l_g)	4 mm
Diameter of N pole (D_{np})	34 mm
Number of turns of coil to electromagnet (N)	3000
Size of workpiece	150 mm × 150 mm ×1.2 mm
Workpiece material	SUS304 stainless steel
Hardness of workpiece (H_m)	5.5 GPa
Shear strength of workpiece (τ_s)	13.28 GPa
Type of abrasive grain	Al_2O_3
Relative permeability of abrasive grain (μ_{rabr})	0.999996
Permeability of free space (μ_0)	$4\pi \times 10^{-7}$ H/m
Volume fraction of iron particle (α)	0.70
RPM of rotating pole (N_{rs})	196
Power input (P)	1 kW
Diameter of abrasive grain (ds)	5 μm
Diameter of magnetic abrasive particle (D_{map})	100 μm
Mean semi angle of surface asperity (θ_w)	80°
Initial surface roughness (R_{max}^0)	1.5 μm
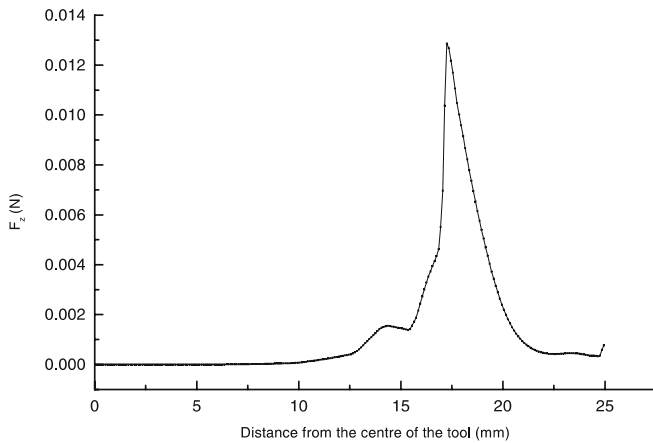
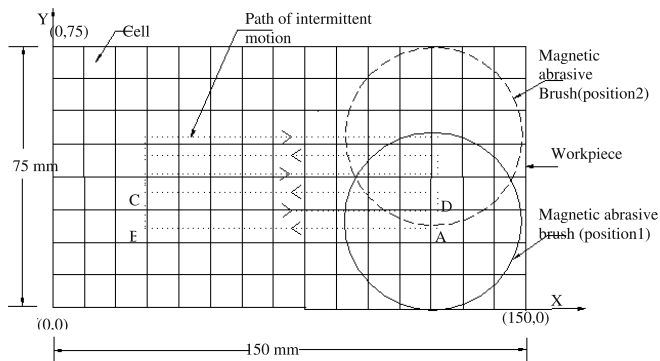**Fig. 11.** Distribution of normal magnetic force for machining conditions given in Table 1

Fig. 13. Variation of surface roughness at various *y*-levels in case of the tool movement along *x*-axis after 126 revolutions

Fig. 12. Schematic diagram of movement of the tool in *x* direction

Fig. 14. Variation of the product of normal magnetic force and contact time of the tool at various *y*-levels in case of the tool movement along *x*-axis. No. of revolutions of the tool = 126

the normal magnetic force is relatively higher near the edge of a magnetic pole in comparison to other parts of the tool. It is due to a larger variation in gradients of the intensity of magnetic field near the edge. Such behavior near the edges is observed experimentally as well (Singh personal communication, 2004).

The size of a cell is taken as 5 mm × 5 mm. Numerical experiments were carried out by providing intermittent motion to the tool in the following two fashions.

(i) Tool movement in the *x* direction and shift in *y* direction
(ii) Tool movement in the *y* direction and shift in *x* direction

(i) Tool movement in the *x* direction and shift in *y* direction

The tool moves from position A to B, then it shifts to location C before it starts moving towards D (Fig. 12). The distance BC is taken to be equal to the cell length. This movement continues till the tool reaches the final position (position 2 of Fig. 12 – one forward pass). The path of the tool center is indicated by a dotted line in Fig. 12. From position 2, the tool returns back to position 1 following the reverse path (– one backward pass).

Figure 13 shows the change in the surface roughness values along the *x*-axis at different *y* levels, after completing one forward pass. It is observed that at various *y* levels, the surface
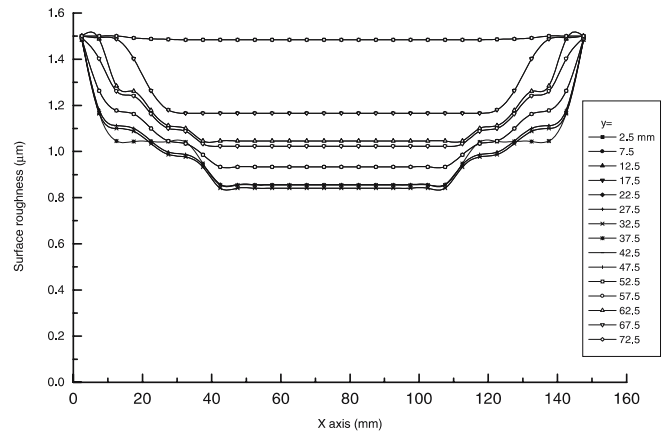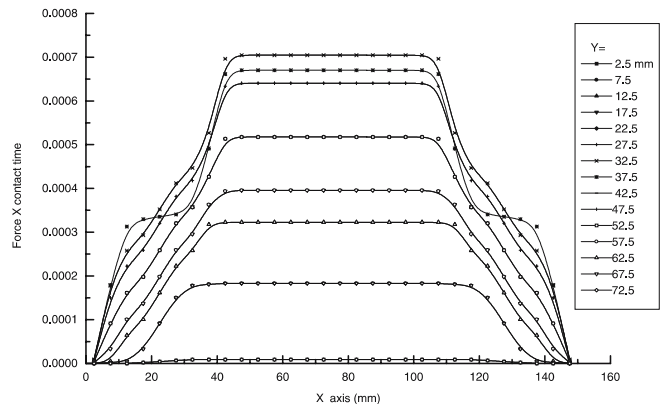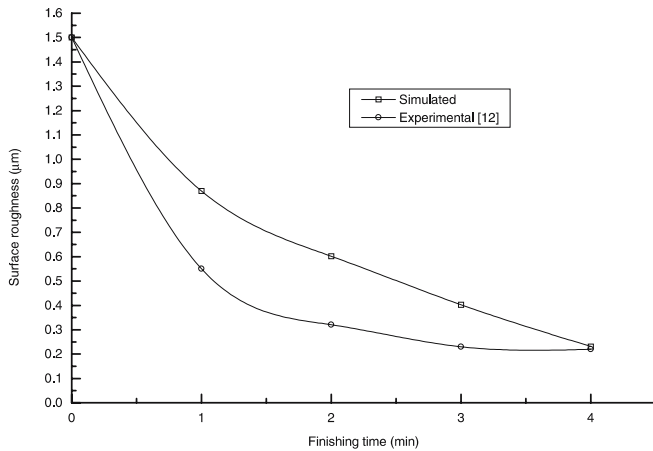
roughness is uniform in a certain region of the workpiece. Note that the normal magnetic force is non-uniform as shown in Fig. 11. However, it is the combined effect of the magnitude of the normal magnetic force and the contact time that is responsible for surface roughness. Figure 14 shows the variation of the product of the magnitude of the normal magnetic force and the contact time along the *x*-axis at different *y* levels. It shows that, at various *y* levels, the product is constant in a certain region of the workpiece surface. Further, one is concave in nature while another is convex in nature. This explains the uniform nature of surface roughness in certain regions of the workpiece surface. The improvement in the surface roughness is less, when "*x*" is either less than 25 mm or more than 125 mm. The same thing is observed, when "*y*" is either 2.5 mm or 72.5 mm. These parts lie in the fringing zones of the brush at the ends of the passes. In the end of fringing zones, the magnetic force almost reaches the zero value, hence this can be called the fringing zone effect. This effect can be reduced by using a dummy workpiece in the fringing zone region. The surface quality of the workpiece at any time is represented as the average of the surface roughness of the cells excluding the cells lying in the region of the fringing

Table 2. Comparison of surface roughness with the experimental results [12]

S. no.	Time (min)	Surface roughness (μm)				% Error			
		Experi-mental	Theoretical						
			Tool movement in x direction	Tool movement in y direction	Tool movement in x direction	Tool movement in y direction			
1.	1	0.55	0.87	0.87	36.78	36.78			
2.	2	0.32	0.60	0.61	46.66	47.54			
3.	3	0.23	0.40	0.40	42.50	42.50			
4.	4	0.22	0.23	0.24	4.34	8.33			

Fig. 15. Comparison of surface roughness with the experimental results [12] in case of the tool movement along x-axis

Fig. 16. Schematic diagram of movement of the tool in y-direction. Movement along Y-axis

Figure 15 and Table 2 show that the simulated values are higher than experimental results, but the trend is the same as that of the experimental results. Initially the discrepancy is higher but it reduces as finishing time increases. This discrepancy may be due to either computational limitations and/or some of the assumptions of the model.

7 Conclusions

In the present investigation, modeling and numerical simulation of surface roughness in the MAF process have been performed. This helps in understanding the mechanism of forces applied and the material removal. The following conclusions are drawn on the basis of the results discussed.

The magnitude of the normal magnetic force is relatively higher near the edge of the magnetic pole due to the edge effect. The surface roughness of the workpiece can be found in almost the same way by providing the intermittent motion to the tool either along the x-axis or y-axis. These simulated results compare favorably well with the experimental results after finishing for a period of 4 min.

Nomenclature

A_p	Projected area of the penetration (m^2)
B	Magnetic flux intensity (T)
D	Electric flux density (C/m^2)
D_{map}	Diameter of a magnetic abrasive particle (m)
D_{np}	Diameter of the N-pole (m)
ds	Diameter of an abrasive particle (m)
E	Electric field intensity (V/m)
E_m	Magnetic potential energy (J)
F_{cedge}	Cutting force available on a cutting edge (N)
F_{zedge}	Normal force acting on a cutting edge (N)
F_{tedge}	Tangential force on a cutting edge (N)
F_{redge}	Radial magnetic force on a cutting edge (N)
H	Magnetic field intensity (A/m)
H_m	Hardness of workpiece material (N/m^2)
hs	Depth of penetration of abrasive particle (m)

zone effects. Table 2 shows a comparison of the surface quality computed as above with experimental results [12] at four discrete times. Figure 15 shows the comparison when the time is varied continuously upto 4 min.

(ii) Tool movement in the y direction and shift in x direction

In this motion, the tool first moves intermittently along the positive y-axis. Starting from position 1 (Fig. 16), it moves a distance equal to the cell breadth after each revolution. Upon reaching the opposite side, the tool shifts along the negative x-axis by a distance equal to the cell length and again it resumes the intermittent motion along the y-axis (this time along the negative y-axis). This sequence is repeated till the tool reaches the final position (position 2 of Fig. 16). When the tool reaches position 2, it completes 126 revolutions and takes 0.64 min. From position 2, the tool returns back to the position 1 following the reverse path. In this way, intermittent motion is provided upto 4 min. It is completed in 784 revolutions of the tool.

The change in the surface roughness is also estimated along the x direction after completing 126 revolutions of the tool, at different y levels. It gives the same results as seen in Fig. 13. The surface quality of the workpiece is compared with the experimental results [12] in Table 2 at four discrete times.
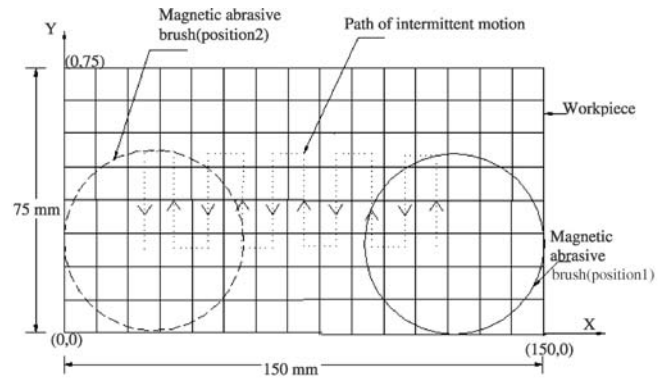
I   Input current to electromagnet (A)
J   Current density (A/m^2)
$[k]^e$ Elemental coefficient matrix
l_g Working gap (m)
l_b Base length of single profile (m)
l_c Length of cell (m)
M   Magnetization of magnetic abrasive particles (A/m)
N   No. of turns in the electromagnet
N_{rs} Rotational speed of the tool (RPM)
n_{rev} Total number of revolution
n_t Total number of tracks
n_a Number of active cutting edges on a magnetic abrasive particle
$n_{ct(tr)}$ Total number of cutting edges on MAPs in track tr-th
n_f Number of profiles in a cell
$R_{(tr)}$ Radius of the tr-th track (m)
R_{max}^0 Initial surface roughness of the workpiece (μm)
r Radius of projected area of indentation (m)
t   Time (s)
ΔA Projected area of indentation (m^2)
α Volume fraction of ferromagnetic particles
ϕ Magnetic potential (AT)
μ_0 Permeability of free space (H/m)
μ_r Relative permeability of magnetic abrasive particle
θ_w Semi-mean angle of surface asperity
μ_{rabr} Relative permeability of abrasive particle.
χ_r Susceptibility of magnetic abrasive particle
$\chi_{r\,ferr}$ Susceptibility of ferromagnetic material
χ_{rabr} Susceptibility of abrasive particle
τ_s Shear strength of workpiece material (N/m^2)
ρ Density of workpiece material (kg/m^3)
i, j   Coordinates x and y
r, θ, z Coordinates r, θ and z
         Superscripts
e   Element
T   Transpose

References

1. Jain VK (2002) Advanced machining processes. Allied Publishers, Delhi
2. Jain VK, Kumar P, Behra PK, Jayswal SC (2001) Effect of working gap and cicumferential speed on the performance of magnetic abrasive finishing process. Wear 250:384–390
3. Yamguchi H, Shinmura T (1999) Study of surface modification resulting from an internal magnetic abrasive finishing. Wear 225:246–255
4. Chang GW, Yan BH, Hsu RT (2002) Study on cylindrical magnetic abrasive finishing using unbonded magnetic abrasives. Int J Mach Tools Manuf 42:575–583
5. Shinmura T, Takazawa K, Hatano E (1986) Study on magnetic abrasive finishing-effects of machining fluid on finishing characteristics. Bull Japan Soc Precis Eng 20(1):52–54
6. Shinmura T, Takazawa K, Hatano E, Matsunaga T (1990) Study on magnetic abrasive finishing. Ann CIRP 39(1):325–328
7. Shinmura T, Takazawa K, Hatano E, Aizawa T (1985) Study on magnetic abrasive process- process principles and finishing possibility. Bull Japan Soc Precis Eng 19(1):54–55
8. Shinmura T, Takazawa K, Hatano E, Aizawa T (1984) Study on magnetic abrasive process- finishing characteristics. Bull Japan Soc Precis Eng 18(4):347–348
9. Shinmura T, Takazawa K, Hatano E (1987) Study on magnetic abrasive – effects of various types of magnetic abrasives on finishing characteristics. Bull Japan Soc Precis Eng 21(2):139–141
10. Fox M, Agrawal K, Shinmura T, Komanduri R (1994) Magnetic abrasive finishing of rollers. Ann CIRP 43(1):181–184
11. Shinmura T, Aizawa T (1989) Study on magnetic abrasive finishing process-development of plane finishing apparatus using a stationary type electromagnet. Bull Japan Soc Precis Eng 23(3):236–239
12. Shinmura T, Takazawa K, Hatano E (1985) Study on magnetic abrasive process-application to plane finishing. Bull Japan Soc Precis Eng 19(4):289–291
13. Hou ZB, Komanduri R (1998) Magnetic field assisted finishing of ceramics-on the thermal aspect of magnetic abrasive finishing of ceramic rollers. Trans ASME J Eng Ind 20:660–667
14. Waigaonkar SD, Navale LG, Kajale SR (2000) Optimization of magnetic abrasive finishing process. Proc 19th AIMTDR Conference, Channai, India, pp 147–152
15. Yamguchi H, Shinmura T (2000) Study on internal magnetic abrasive finishing using a pole rotation system-discussion of characteristics abrasive behaviour. Precis Eng 24:237–244
16. Kremen GZ, Elsayed EA, Ribeiro JL (1994) Machining time estimation for magnetic abrasive processes. Int J Prod Res 32(12):2817–1825
17. Kim J, Choi M (1995) Simulation for the prediction of surface-accuracy in magnetic abrasive machining. J Mater Process Technol 53:630–642
18. Kremen GZ, Elsayed EA, Rafalorich VI (1996) Mechanism of material removal in magnetic abrasive process and the accuracy of machining. Int J Prod Res 34(9):2629–2638
19. Jefimenko OD (1966) Electricity and magnetism. Meridith, New York
20. Reddy JN (1993) An introduction to the finite element method, 2nd ed. McGraw-Hill, New Delhi
21. Griffiths DV, Smith IM (1991) Numerical methods for engineers. Blackwell Scientific, Oxford
22. Stradling AW (1993) The physics of open-gradient dry magnetic separation. Int J Miner Process 39:1–18
23. Mulay LN (1963) Magnetic susceptibility. Wiley, New York
24. Rabinowicz E, Dunn LA, Russel PG (1961) A study of abrasive wear under three-body conditions. Wear 4:345–355
25. Edminister JA (1986) Theory and problems of electromagnetics. McGraw-Hill, New York

Appendix – I
Relationship between $\mu_{r\,ferr}$ and H, $\chi_{r\,ferr}$ and H

The graphical relationship between the relative permeability $\mu_{r\,ferr}$ and field strength **H** of the ferromagnetic material [25] is shown in Fig. 17. It shows a highly non-linear behavior. Therefore, to find out the mathematical expression between $\mu_{r\,ferr}$ and H with minimum possible error, the graphical representation is divided into three regions as indicated in Fig. 17. The expressions for these three regions are obtained as given below. In the following expressions, H is the magnitude of the vector **H**.

(a) For region I:

$$\mu_{r\,ferr} = 743.4520 + 16.1679\,H + 0.7794\,H^2 \tag{52}$$

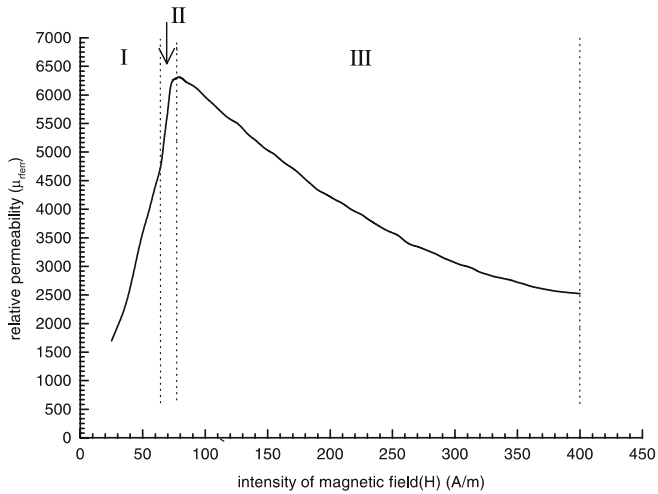$$\chi_{r\,ferr} = 742.4520 + 16.1679\,H + 0.7794\,H^2 \tag{53}$$

Fig. 17. Relationship between relative permeability and intensity of magnetic field

(b) For region II:

$$\mu_{r\,ferr} = -247748.4573 + 9689.6642\,H$$
$$- 123.2216\,H^2 + 0.5224\,H^3 \tag{54}$$

$$\chi_{r\,ferr} = -247749.4573 + 9689.6642\,H$$
$$- 123.2216\,H^2 + 0.5224\,H^3 \tag{55}$$

(c) For region III:

$$\mu_{r\,ferr} = 8231.1280 - 25.6849\,H + 0.0283\,H^2 \tag{56}$$
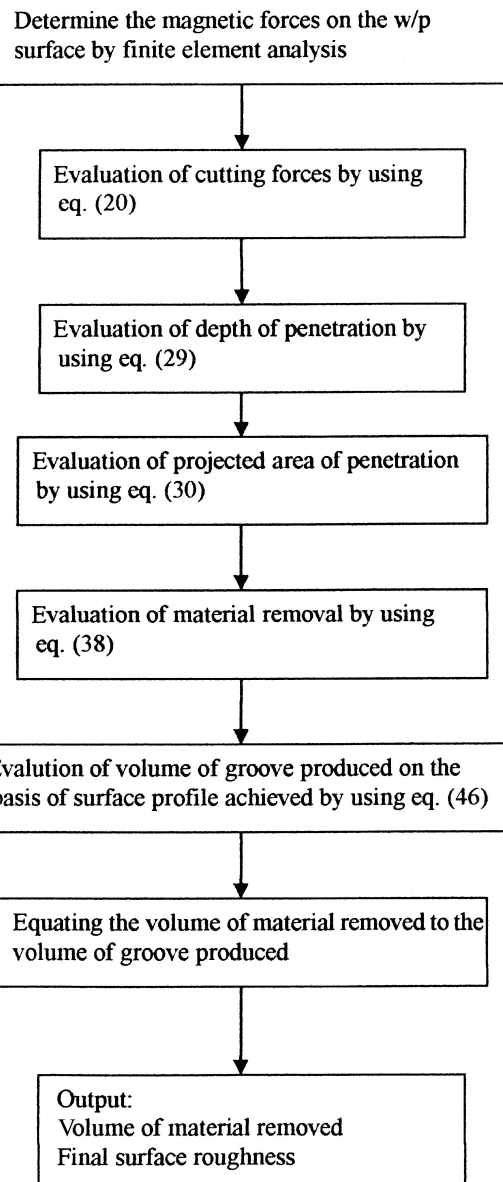
$$\chi_{r\,ferr} = 8230.1280 - 25.6849\,H + 0.0283\,H^2 \tag{57}$$

After region III, the saturation region starts. In this region, the susceptibility and relative permeability remain constant. These are found by substituting the value of H at the saturation point in the expressions of region III. In the present case, saturation occurs at the value of $H = 400\,A/m$.

Appendix – II
Flow chart for determination of material removal and surface roughness

Input:
material properties of w/p
size of w/p, size of MAP, size of abrasive particle,
volume fraction, flux density, properties of MAP,
power input, RPM of rotating pole, finishing time,
initial surface roughness of w/p

Determine the magnetic forces on the w/p surface by finite element analysis

Evaluation of cutting forces by using eq. (20)

Evaluation of depth of penetration by using eq. (29)

Evaluation of projected area of penetration by using eq. (30)

Evaluation of material removal by using eq. (38)

Evalution of volume of groove produced on the basis of surface profile achieved by using eq. (46)

Equating the volume of material removed to the volume of groove produced

Output:
Volume of material removed
Final surface roughness

Appendix – III
Computation of surface roughness in 2nd and 3rd revolutions

(i) 2nd revolution:

Cross sectional area of material (BCFE) removed in the 2nd revolution is obtained from the geometry of the profile of the workpiece surface as shown in Fig. 10.

Cross sectional area of BCFE =

$$\left[\left(R_{max}^0 - R_{max(i,j)}^{(2)}\right)^2 - \left(R_{max}^0 - R_{max(i,j)}^{(1)}\right)^2\right]\tan\theta_w \tag{58}$$

The volume of material removed in cell (i,j) by a cutting edge in the 2nd revolution is given by

$$\Delta Vg_{ed(i,j)}^{(2)} = \text{Cross sectional area of BCFE} \times r_{(tr)} \times n_f \qquad (59)$$

Substituting the value of the cross sectional area of BCFE from Eq. 58 and n_f from Eq. 45 in Eq. 59,

$$\Delta Vg_{ed(i,j)}^{(2)} = \frac{\left(\left(R_{max}^0 - R_{max(i,j)}^{(2)} \right)^2 - \left(R_{max}^0 - R_{max(i,j)}^{(1)} \right)^2 \right) r_{(tr)} l_c}{2 R_{max}^0} \qquad (60)$$

The total volume of material removed in cell (i,j) by "$n_{(tr)}$" particles in the 2nd revolution is given by

$$\Delta Vg_{(i,j)}^{(2)} = \frac{\left(\left(R_{max}^0 - R_{max(i,j)}^{(2)} \right)^2 - \left(R_{max}^0 - R_{max(i,j)}^{(1)} \right)^2 \right) r_{(tr)} l_c \pi R_{(tr)} n_a}{R_{max}^0 D_{map}} \qquad (61)$$

Equating the volume of material removed $\left(\Delta V_{(i,j)}^{(2)} \right)$ to the groove produced $\left(\Delta Vg_{ed(i,j)}^{(2)} \right)$ in cell (i,j) in 2nd revolution, we get

$$R_{max(i,j)}^{(2)} =$$

$$R_{max}^0 - \left(\left(R_{max}^0 - R_{max(i,j)}^{(1)} \right)^2 + \left(\frac{\Delta V_{(i,j)}^{(2)} R_{max}^0 D_{map}}{\pi r_{(tr)} l_c R_{(tr)} n_a} \right) \right)^{\frac{1}{2}} \qquad (62)$$

(ii) 3rd revolution:

The cross sectional area of material (EFIH) removed in the 3rd revolution is obtained from geometry of the profile of the workpiece surface as shown in Fig. 10.

Cross sectional area of EFIH =

$$\left[\left(R_{max}^0 - R_{max(i,j)}^{(3)} \right)^2 - \left(R_{max}^0 - R_{max(i,j)}^{(2)} \right)^2 \right] \tan \theta_w \qquad (63)$$

The volume of material removed in cell (i,j) by a cutting edge in the 3rd revolution is given by

$$\Delta Vg_{ed(i,j)}^{(3)} = \text{Cross sectional area of EFIH} \times r_{(tr)} \times n_f \qquad (64)$$

Substituting the value of the cross sectional area of EFIH from Eq. 63, n_f from Eq. 45 in Eq. 64,

$$\Delta Vg_{ed(i,j)}^{(3)} = \frac{\left(\left(R_{max}^0 - R_{max(i,j)}^{(3)} \right)^2 - \left(R_{max}^0 - R_{max(i,j)}^{(2)} \right)^2 \right) r_{(tr)} l_c}{2 R_{max}^0} \qquad (65)$$

The total volume of the groove produced in cell (i,j) by "$n_{(tr)}$" particles in the 3rd revolution is given by

$$\Delta Vg_{(i,j)}^{(3)} = \frac{\left(\left(R_{max}^0 - R_{max(i,j)}^{(3)} \right)^2 - \left(R_{max}^0 - R_{max(i,j)}^{(2)} \right)^2 \right) r_{(tr)} l_c \pi R_{(tr)} n_a}{R_{max}^0 D_{map}} \qquad (66)$$

Equating the volume of material removed $\left(\Delta V_{(i,j)}^{(3)} \right)$ to the groove produced $\left(\Delta Vg_{ed(i,j)}^{(3)} \right)$ in cell (i,j) 3rd revolution, we get

$$R_{max(i,j)}^{(3)} =$$

$$R_{max}^0 - \left(\left(R_{max}^0 - R_{max(i,j)}^{(2)} \right)^2 + \left(\frac{\Delta V_{(i,j)}^{(3)} R_{max}^0 D_{map}}{\pi r_{(tr)} l_c R_{(tr)} n_a} \right) \right)^{\frac{1}{2}} \qquad (67)$$